HHS Public Access

Author manuscript

Nat Struct Mol Biol. Author manuscript; available in PMC 2022 February 09.

Published in final edited form as:

Nat Struct Mol Biol. 2021 August ; 28(8): 671–680. doi:10.1038/s41594-021-00635-0.

Structure of a meiosis-specific complex central to BRCA2 localization at recombination sites

Devon F. Pendlebury[1,2,3,#], **Jingjing Zhang**[4,#], **Ritvija Agrawal**[1], **Hiroki Shibuya**[4,*], **Jayakrishnan Nandakumar**[1,2,*]

[1]Department of Molecular, Cellular, and Developmental Biology, University of Michigan, Ann Arbor, MI, USA;

[2]Program in Chemical Biology, University of Michigan, Ann Arbor, MI 48109, USA;

[3]current address: Pharmaceutical Sciences, University of California Irvine, Irvine, CA, USA;

[4]Department of Chemistry and Molecular Biology, University of Gothenburg, Gothenburg, Sweden.

Abstract

Meiotic cells invoke BRCA2 to repair programmed double-stranded DNA breaks to accomplish homologous recombination. The meiosis-specific protein MEILB2 facilitates BRCA2 recruitment to meiotic recombination sites. Here, we combine crystallography, biochemical analysis, and a mouse meiosis model to reveal a robust architecture that ensures meiotic BRCA2 recruitment. The crystal structure of the MEILB2-BRCA2 complex reveals how two MEILB2 homodimers sandwich two chains of BRCA2 to afford a 4:2 architecture. The sandwich lacks close contact between the two MEILB2 dimers or the two BRCA2 chains. Instead, the two halves of each BRCA2 chain bridge two MEILB2 subunits from different homodimers to form the MEILB2-BRCA2-MEILB2 sandwich. Several identical residues from the two MEILB2 subunits are employed to engage the BRCA2 halves, justifying their strict conservation. Mutational analysis of the interface reveals a synergistic mechanism for MEILB2-BRCA2 recruitment during meiosis. Overall, these studies demonstrate how BRCA2 efficiently localizes in the cell to facilitate meiosis.

[*]**Correspondence:** jknanda@umich.edu and hiroki.shibuya@gu.se. **Correspondence and requests for materials** should be addressed to J.N. and H.S.

Author Contributions Statement. J.N., D.F.P. and H.S. designed the study. Crystallography was performed by D.F.P. and J.N. R.A. and D.F.P. performed *in vitro* validation of the structural interface. J.J. performed the *in vivo* validation of the structural interface with help from H.S. All authors were involved in data analysis. J.N., D.F.P., and H.S. wrote the manuscript with critical feedback from the remaining authors.

[#]denote equally contributing authors.

Competing Interests Statement. The authors declare no competing financial interests.

Supplementary Information is available for this manuscript.

Statistics: Details of statistics, including number of observations and criteria used for calculating statistical significance, is indicated in the relevant figure legends.

Introduction

Breast cancer susceptibility gene 2 (BRCA2) plays a central role in the homologous recombination (HR) pathway of DNA repair that uses the sequence of an intact sister chromatid to template the repair of double-stranded breaks (DSBs) in an error-free fashion[1–4]. HR is an essential determinant of genomic integrity and defects in this pathway are strongly associated with tumor development[5–7]. Indeed, BRCA2 is best known for germline mutations that pose a major risk for developing both breast and ovarian cancers[8]. The MRN (MRE11-RAD50-NBS1) exonuclease complex[9,10] resects DSBs into single-strand DNA (ssDNA), which is coated by the RPA (Replication Protein A) heterotrimeric complex[11]. BRCA2 then replaces RPA with the RAD51 recombinase to promote RAD51 nucleoprotein filament formation, strand exchange, and DSB repair[12]. Mutation of BRCA2 or other genes that are part of the HR machinery disrupts the high-fidelity HR pathway, leaving the cell to rely on the error-prone NHEJ (non-homologous end-joining) pathway to repair DSBs[13].

While HR in mitotic cells counters accidental DNA damage events, it is a central part of the normal physiology of cells in the germline that are undergoing meiosis. Genetic crossover, which is the product of HR between paternally- and maternally-derived homologous chromosomes in cells undergoing meiosis, is critical for the proper segregation of chromosomes and promotion of genetic diversity[14]. Improper segregation results in aneuploidy, which is a major risk factor for infertility, miscarriages, and birth defects[15]. Meiotic and mitotic HR share several factors, including MRN, RPA, BRCA2, and RAD51, but unique challenges posed by meiosis invoke the need for additional factors and adaptations. One such challenge is the widespread programmed DSB formation in meiosis, catalyzed by the meiosis-specific topoisomerase-like SPO11 enzyme with its partner protein TOPVIBL and distributed throughout the genome[16–18]. In contrast to the sporadic DNA lesions encountered in most somatic cells, repair of the abundant meiotic DSBs would require efficient recruitment of the DNA DSB-repair machinery in a narrow time-frame.

Recent work has highlighted the critical importance of a meiosis-specific armadillo (ARM) repeat-containing protein called MEILB2 (meiotic localizer of BRCA2; previously called HSF2BP) with no known mitotic HR counterpart[19]. MEILB2 associates with the meiosis-specific ssDNA-binding MEIOB-SPATA22 complex and localizes to sites of meiotic HR[20]. MEILB2 is critical for recruiting BRCA2 to recombination nodules in mouse spermatocytes, providing a robust mechanism to coat BRCA2 on the DSBs spread across the genome[19]. Knockout of MEILB2 eliminates not only BRCA2 but also RAD51 and DMC1 (a meiosis-specific paralog of RAD51) from meiotic DSBs, leading to erroneous DSB repair and male sterility[19]. Thus, MEILB2, like SPO11, represents a category of proteins that performs a function exclusive to meiotic HR.

Full-length MEILB2 protein is homodimeric but highly aggregation-prone due to an extended coiled-coil region at its N-terminus (Fig. 1A). A meiosis-specific coiled-coil accessory protein BRME1 binds the N-terminal coiled-coil of MEILB2 in a 2:2 stoichiometry to stabilize its homodimeric state[20]. BRCA2 binds to the ARM repeat domain of MEILB2 that is downstream of its N-terminal coiled-coil[19,21] (Fig. 1A). Indeed,

truncating the MEILB2 N-terminus (mouse MEILB2$^{87\text{-end}}$) reduces aggregation to afford a stable MEILB2 homodimer that forms a complex with BRCA2[20]. Interestingly, human MEILB2 R200 in the ARM domain emerged as the sole hit from a mutagenesis screen to map BRCA2-binding residues, suggesting a robust interface between the two proteins[21]. The MEILB2-binding region of human BRCA2 was mapped to a short stretch (G2270-T2337; BRCA2^{MBD}) that is outside of its known functional domains (Fig. 1A).

Mouse MEILB2$^{87\text{-end}}$ is a homodimer but its binding to BRCA2^{MBD} results in a homogenous complex with unusual stoichiometry[20]. Using size-exclusion chromatography-coupled multi-angle light scattering (SEC-MALS), we made the surprising observation that this complex contains four copies of mouse MEILB2$^{87\text{-end}}$, suggesting that BRCA2 binding transforms the quaternary state of MEILB2[20]. However, the structural basis for this unique stoichiometry or its physiological consequences remains unknown. Here, we solve the structure of the human MEILB2$^{83\text{-end}}$-BRCA2^{MBD} complex to reveal a novel 4:2 structural mechanism for BRCA2 recruitment to meiotic DSBs that involves an unusual combination of canonical and inverted ARM repeats for MEILB2 homodimerization, a series of salt-bridges that sandwich BRCA2 between MEILB2 dimers, and MEILB2-BRCA2 stacking interactions that reinforce MEILB2 homodimerization. Disruption of the MEILB2-BRCA2 interface with mutations disassembles the complex *in vitro* and compromises both MEILB2 and BRCA2 recruitment to meiotic DSBs *in vivo*. Together, our results uncover a unique structural architecture that underlies efficient BRCA2 recruitment to sites of recombination during meiotic HR, a step that is indispensable for crossover, the proper segregation of chromosomes, and fertility.

Results

Human MEILB2$^{83\text{-end}}$ -BRCA2^{MBD} forms a 4:2 complex

We previously demonstrated that mouse BRCA2^{MBD} binds MEILB2$^{87\text{-end}}$ to transform the MEILB2 homodimer to a complex containing four copies of this protein[20]. Recombinantly co-expressed human homologs of these protein constructs, namely, human MEILB2$^{83\text{-end}}$ and BRCA2^{MBD} (aa 2271–2335), co-eluted from a size-exclusion column (SEC) consistent with complex formation (Fig. 1A,B). SEC-MALS of the purified human MEILB2$^{83\text{-end}}$-BRCA2^{MBD} complex was not only consistent with four copies of the MEILB2$^{83\text{-end}}$ protein in the complex but further revealed the presence of two BRCA2^{MBD} copies to yield an assembly with 4:2 composition (Fig. 1C).

Overall structure of human MEILB2$^{83\text{-end}}$ -BRCA2^{MBD}

We solved the X-ray crystal structure of the human MEILB2$^{83\text{-end}}$-BRCA2^{MBD} complex at 2.56 Å resolution using single-wavelength anomalous diffraction of a selenomethionine derivative (Table 1). The asymmetric unit (ASU) contains two copies of MEILB2$^{83\text{-end}}$ and one copy of BRCA2^{MBD} (aa 2286–2335) (Fig. 1D). Each MEILB2$^{83\text{-end}}$ chain contains tandem ARM repeats that immediately follow a long α-helix at the N-terminus. The MEILB2$^{83\text{-end}}$ subunits homodimerize using non-crystallographic symmetry (NCS). The two MEILB2$^{83\text{-end}}$ subunits are asymmetric (named “A” and “B”) as only one of them (B) associates with BRCA2^{MBD} in the ASU. The entire BRCA2^{MBD} chain was highly

ordered ($2F_o$-F_c map; Ext. data fig. 1) despite lacking any obvious secondary structural elements (Fig. 1D). Nevertheless, only a fraction of BRCA2^{MBD} was associated with the MEILB2$^{83\text{-end}}$ B subunit in the ASU. The unsatisfied binding valency of BRCA2$^{83\text{-end}}$ suggested that the biological assembly involved more than one ASU.

Analysis of the interactions between all the ASUs in the unit cell (by the PISA program[22]) revealed that the inclusion of a symmetry mate (i.e., an identical copy of the BRCA2^{MBD} -MEILB2$^{83\text{-end}}$ A-B complex that is related to it by crystallographic two-fold symmetry) would result in a 4:2 complex that accounts for MEILB2$^{83\text{-end}}$ binding throughout the BRCA2^{MBD} chain and is consistent with the biological assembly observed in solution (Fig. 1E–G). We call the MEILB2$^{83\text{-end}}$ subunits in the symmetry mate “a” and “b” as they are structurally identical to MEILB2$^{83\text{-end}}$ A and B subunits, respectively. The biological assembly brings together two homodimers of MEILB2$^{83\text{-end}}$ and two BRCA2^{MBD} monomers in a 4:2 stoichiometry. However, the two MEILB2$^{83\text{-end}}$ homodimers do not directly bind each other; neither do the two BRCA2^{MBD} chains interact directly with each other. Instead, the two MEILB2$^{83\text{-end}}$ dimers are stitched together by the two BRCA2^{MBD} chains (schematic in Fig. 1E; structures in Fig. 1F,G and Ext. data fig. 2B,C). The BRCA2^{MBD} chains linking MEILB2$^{83\text{-end}}$ A and b, and a and B, were accordingly named BRCA2^{MBD} (Ab) and BRCA2^{MBD} (aB), respectively. The tight interactions between the subunits within each MEILB2$^{83\text{-end}}$ homodimer and between the MEILB2$^{83\text{-end}}$ homodimers and BRCA2^{MBD} result in a compact assembly (the total solvent-accessible area that is buried upon the formation of the 4:2 complex = 15,685 Å^2), consistent with lower B-factors at these interfaces in the crystal structure (Ext. data fig. 2A). The ASU also contains a short peptide (^{2276}PLILVGE^{2282}; *; black or grey in Fig. 1D,F,G) derived from an adjacent BRCA2^{MBD} molecule in the crystal lattice (Ext. data fig. 2D,E and Methods). The short peptide does not participate in MEILB2 homodimerization or MEILB2-BRCA2 interaction but is rather involved in making BRCA2-BRCA2 lattice contacts (Ext. data fig. 2D,E and Methods). BRCA2^{MBD} lacking ^{2276}PLILVGE^{2282} (ΔPLILVGE) binds MEILB2$^{83\text{-end}}$ and forms a 4:2 MEILB2:BRCA2 complex like wild type BRCA2^{MBD}, suggesting that the crystal contacts made by this peptide are not necessary for MEILB2-BRCA2 quaternary structure (Ext. data fig. 2F,G). As both full-length MEILB2 and MEILB2$^{83\text{-end}}$ are homodimeric[20], and as full-length BRCA2 has also been shown to be homodimeric[23], our structure is consistent with one BRCA2 homodimer being recruited by two MEILB2 homodimers to meiotic DSBs.

Adaptation of ARM repeats in MEILB2 homodimerization

The homodimeric interface of MEILB2$^{83\text{-end}}$ is structurally novel and is mediated via interactions between the long N-terminal helix in each subunit and the first ARM repeat of the other subunit (Fig. 2A). While the first ~three turns of the N-terminal helix of each MEILB2$^{83\text{-end}}$ are only weakly associated with the dimeric partner (note higher B-factors for this region; Ext. data fig. 2A), the interaction solidifies with the help of an intermolecular disulfide bridge formed between the Cys120 residues of each subunit (Fig. 2A,B). Downstream of this residue, the core of the homodimerization interface is facilitated by hydrophobic residues L130, L131, I144, and F153 from each MEILB2$^{83\text{-end}}$ subunit (Fig. 2C). An exception to this theme is a salt-bridge between K152 and E122 of the two subunits

in the homodimer. The homodimerization of MEILB2$^{83\text{-end}}$ is consistent with our prior SEC-MALS analysis of this complex in the absence of BRCA2[20]. Our results suggest that the long N-terminal helix of the ARM domain of MEILB2 is an extension of the N-terminal coiled-coil domain of full-length MEILB2 (aa 14–118 of human MEILB2; (Fig. 1A)) that is known to mediate dimerization and bind to BRME1 in a 2:2 stoichiometry[20].

A DALI search for structural homologs with the MEILB2$^{83\text{-end}}$ B subunit fetched β-catenin, the prototypical ARM repeat protein (armadillo is the *Drosophila melanogaster* homolog of β-catenin), as the top hit (Ext. data fig. 3A–D; PDB ID: 1i7w, Z-score = 19, rmsd = 6.2 Å). Alignment of the B subunit of the MEILB2$^{83\text{-end}}$ AB homodimer and β-catenin structure highlighted their structural homology despite the shorter domain length of MEILB2$^{83\text{-end}}$ (Ext. data fig. 3D). Although MEILB2$^{83\text{-end}}$ A was not included in the alignment operation, its ARM repeats superimpose with β-catenin ARM repeats that are immediately upstream (i.e., N-terminal) of the alignment region with MEILB2$^{83\text{-end}}$ B (Ext. data fig. 3E,F). The orientation of MEILB2$^{83\text{-end}}$ A to β-catenin revealed that their ARM repeat helices overlay with each other with opposite N→C polarity (Ext. data fig. 3G), suggesting that MEILB2$^{83\text{-end}}$ combines canonical and inverted ARM repeats to form a homodimer that mimics the fold of β-catenin.

Salt-bridges drive BRCA2 sandwiching

The interactions of BRCA2 with its two MEILB2 partners are dominated by polar interactions, including a large number of ionic interactions (Ext. data fig. 4). However, the MEILB2-BRCA2-MEILB2 sandwich is asymmetric as the MEILB2$^{83\text{-end}}$ a/A - BRCA2^{MBD} interface is much more extensive than the MEILB2$^{83\text{-end}}$ B/b - BRCA2^{MBD} interface (Fig. 2D and Ext. data fig. 4). In MEILB2$^{83\text{-end}}$ a/A, positively-charged R200 forms a salt-bridge with BRCA2^{MBD} D2294 (Fig. 2D and Ext. data fig. 5A). Besides, there are three salt-bridges formed between negatively charged residues in MEILB2$^{83\text{-end}}$ a/A and positively charged residues in BRCA2^{MBD}: D326 with K2302, D268/E270 with R2319, and E285 with R2295 (Fig. 2D and Ext. data fig. 5C,E,F). In addition to these electrostatic interactions, there is a stacking interaction between MEILB2$^{83\text{-end}}$ a/A W132 and BRCA2^{MBD} P2311 that further bolsters the interface (Fig. 2D and Ext. data fig. 5G; and see discussion later).

Comparison of the two halves of the MEILB2-BRCA2-MEILB2 sandwich interface revealed that several amino acids, including R200, D326, and W132 in MEILB2$^{83\text{-end}}$, are used by both MEILB2$^{83\text{-end}}$ a/A and B/b to bind different regions of BRCA2^{MBD}. MEILB2 R200 forms salt-bridges with BRCA2^{MBD} D2294 (in case of MEILB2$^{83\text{-end}}$ a/A) and BRCA2^{MBD} D2317 (in case of MEILB2$^{83\text{-end}}$ B/b) (Ext. data fig. 5A,B). The dual functionality of MEILB2 R200 revealed by our structure provides an elegant explanation for why this residue was the only hit in a previous mutagenesis screen for BRCA2-interacting residues[21]. MEILB2 D326 from both MEILB2$^{83\text{-end}}$ subunits is also involved in electrostatic interactions but two observations suggest that these interactions are weaker (i.e., less ionic) than those mediated by R200 (Ext. data fig. 5C,D). First, MEILB2 a/A D326 is positioned to bind BRCA2^{MBD} K2302, but the electron density for this lysine side-chain is poorly defined (Ext. data fig. 5C). Second, MEILB2 B/b D326 interacts with BRCA2^{MBD} H2324, a

histidine side-chain that is likely uncharged at physiological pH (pK_a of histidine side-chain = 6.0) (Ext. data fig. 5D).

MEILB2 W132 residues stacks against BRCA2^{MBD} P2311 (in case of MEILB2$^{83\text{-end}}$ a/A) and BRCA2^{MBD} P2334 (in case of MEILB2$^{83\text{-end}}$ B/b) (Fig. 2D and Ext. data fig. 5G,H). Interestingly, W132 is adjacent to residues L130 and L131 in the N-terminal helix of the MEILB2$^{83\text{-end}}$ that forms the crux of the homodimerization interface (Fig. 2C). Inspection of the homodimeric interface of MEILB2$^{83\text{-end}}$ AB in the context of the MEILB2-BRCA2 complex revealed that MEILB2 W132 from the A and B subunits face away from the MEILB2$^{83\text{-end}}$ AB homodimerization core, and stack against BRCA2^{MBD} proline residues to bracket the N-terminal dimerization core (Fig. 2E).

In addition to R200, D326, and W132, several other amino acids (N192, Y238, N239, S241, I242, L244, and S281) are employed by both MEILB2 subunits to H-bond with BRCA2 (Ext. data fig. 4). Together, the structural observations suggest that BRCA2 binding not only helps bring together two MEILB2$^{83\text{-end}}$ dimers but also bolsters interactions between MEILB2$^{83\text{-end}}$ subunits within each homodimer. In agreement with our structural analysis, the residues involved in the MEILB2-BRCA2 and MEILB2-MEILB2 interfaces are highly conserved (Ext. data fig. 5I,J).

Interface mutations cause MEILB2-BRCA2-MEILB2 dissociation

We introduced mutations in the context of MEILB2$^{83\text{-end}}$ and BRCA2^{MBD} to evaluate the importance of the MEILB2-BRCA2 interface observed in our crystal structure. For this, we conducted FLAG co-immunoprecipitation (co-IP) analysis of lysates from HEK 293T cells transiently co-expressing exogenous FLAG-tagged MEILB2$^{83\text{-end}}$ and myc-eGFP-tagged BRCA2^{MBD} that harbor mutations in the MEILB2-BRCA2 interface. FLAG-tagged MEILB2$^{83\text{-end}}$ efficiently pulled down myc-eGFP-tagged BRCA2^{MBD} on anti-FLAG beads (lane #2; Fig. 3A). The association is specific as myc-eGFP-tagged BRCA2^{MBD} did not associate with anti-FLAG beads in the absence of FLAG-tagged protein or presence of FLAG-eGFP (lane #1 in Fig. 3A and Ext. data fig. 6A). Charge-reversal mutations of the bifunctional MEILB2 R200 residue or its binding partners, BRCA2 residues D2294 and D2317, abrogated the MEILB2-BRCA2 interaction (Fig. 3A,B). Mutation of MEILB2 D268 or its salt-bridge partner BRCA2 R2319 also prevented complex formation (Fig. 3A,B). Mutation of MEILB2 W132 that stacks against BRCA2 proline residues P2311 and P2334 eliminated the interaction, confirming the importance of this hydrophobic interaction in the primarily ionic protein-protein interface. Mutation of MEILB2 D326 to H or of its binding partner BRCA2 H2324 to D did not eliminate the MEILB2-BRCA2 interaction. As these mutations would retain polar, uncharged side-chains capable of H-bonding with the wild type partner protein, our results are consistent with MEILB2 D326 participating in H-bonding, as opposed to ionic/salt-bridging interactions, with its BRCA2 binding partners.

We were unable to purify MEILB2$^{83\text{-end}}$ containing mutations in the homodimerization interface using recombinant expression in *E. coli*, suggesting that the mutations compromise protein stability. While this technical limitation prevented us from performing direct MEILB2-MEILB2 binding experiments, validation of the homodimerization using co-IPs was also complicated as two MEILB2$^{83\text{-end}}$ molecules may be bridged by endogenous

BRCA2 even in the absence of MEILB2-MEILB2 dimerization. Indeed, co-IP of FLAG-tagged MEILB2$^{83\text{-end}}$ containing mutations in the homodimerization interface retained association with myc-tagged MEILB2$^{83\text{-end}}$ (Ext. data fig. 6B). To further test the BRCA2 bridging model, we supplemented our co-IPs with transiently overexpressed myc-eGFP-BRCA2^{MBD}. Supplementation of BRCA2^{MBD} allowed for further enrichment of myc-MEILB2$^{83\text{-end}}$ in the FLAG-MEILB2$^{83\text{-end}}$ IP (Ext. data fig. 6C) that was not eliminated by mutations in the homodimerization interface (Ext. data fig. 6D). These results suggest that BRCA2 may bridge MEILB2 molecules even in the absence of efficient homodimerization.

To further understand the role of BRCA2 bridging in MEILB2 ARM domain self-association, we asked how mutations in the MEILB2$^{83\text{-end}}$ -BRCA2^{MBD} interface impact MEILB2$^{83\text{-end}}$-MEILB2$^{83\text{-end}}$ co-IP. MEILB2 and BRCA2 interface mutations were introduced in the context of FLAG-MEILB2$^{83\text{-end}}$ and myc-eGFP-BRCA2^{MBD}, respectively. The mutations eliminated BRCA2^{MBD} pull-down as expected (Fig. 3C,D). All MEILB2$^{83\text{-end}}$ -BRCA2^{MBD} interface mutations, including mutation of MEILB2 W132 that helps lock in the MEILB2$^{83\text{-end}}$ homodimerization interface, also abolished MEILB2$^{83\text{-end}}$ -MEILB2$^{83\text{-end}}$ association (Fig. 3C,D). The complete loss of MEILB2 ARM -MEILB2 ARM association observed here contrasts the binding retained with MEILB2$^{83\text{-end}}$ homodimerization interface mutants, providing compelling evidence that stable association between MEILB2 ARM domains requires intact binding with BRCA2. These results suggest a highly synergistic mode of MEILB2$^{83\text{-end}}$ -BRCA2^{MBD} quaternary structure formation.

Our co-IP was conducted under highly stringent conditions (including 0.02% sodium dodecyl sulfate in the binding buffer) to overcome the non-specific pull-down of MEILB2 on empty beads (driven likely by its hydrophobicity). Accordingly, MEILB2-BRCA2 and MEILB2-MEILB2 binding diminished with single mutations in either half of the BRCA2^{MBD}. To gain further insights into the relative contributions of BRCA2^{MBD} halves to MEILB2 binding, we purified recombinant MEILB2$^{83\text{-end}}$ -BRCA2^{MBD} containing either BRCA2^{MBD} D2294R or D2317R and performed biochemical analysis under less stringent conditions (i.e., native buffer conditions and higher protein complex concentration; 30–50 μM). MEILB2$^{83\text{-end}}$ -BRCA2^{MBD} D2294R eluted from a size-exclusion column like wild type complex and there was no evidence from SEC-MALS for dissociation/destabilization of the 4:2 quaternary structure (Ext. data fig. 7A–C,E). In contrast, two discrete peaks emerged from size-exclusion analysis of MEILB2$^{83\text{-end}}$ -BRCA2^{MBD} D2317R, one corresponding to a 4:2 complex and another to free MEILB2$^{83\text{-end}}$ (Ext. data fig. 7A,D). These data are consistent with structural observations showing a more extensive interface between the BRCA2^{MBD} segment containing D2294 and MEILB2$^{83\text{-end}}$ (subunit A) than between the BRCA2^{MBD} half containing D2317 and MEILB2$^{83\text{-end}}$ (subunit B) (Fig. 2D and Ext. data fig. 4). Moreover, the absence of intermediate stoichiometry (i.e., 2:1) for MEILB2$^{83\text{-end}}$ -BRCA2^{MBD} D2317R suggests a highly cooperative, all-or-none binding mode for the MEILB2-BRCA2 complex.

Interface mutations disrupt MEILB2 and BRCA2 localization

We have previously shown that the localization of BRCA2 at meiotic recombination sites depends on the BRCA2^{MBD} region[19]. To determine the physiological importance of the

MEILB2$^{83\text{-end}}$ -BRCA2^{MBD} interaction captured in our crystal structure, we expressed GFP fusions of mouse BRCA2^{MBD} wild type and mutant proteins (mouse equivalents of human BRCA2^{MBD} mutations in the MEILB2-BRCA2 interface) in mouse spermatocytes by *in vivo* electroporation and examined their subcellular localization. Consistent with previous observations, GFP-BRCA2^{MBD} was visible as punctate foci distributed along the chromosomal axis (stained by SYCP3), which represent meiotic recombination sites (Fig. 4A). However, the introduction of D2242R and D2265R point mutations (equivalent to human BRCA2 D2294R and D2317R, respectively) significantly reduced the signal intensities of the GFP foci (29% and 43% reductions, respectively, compared to wild type; Fig. 4A). D2265R was more deleterious than D2242R, consistent with the biochemical analysis of mutations of the equivalent residues in human BRCA2 (Ext. data fig. 7) and structural data showing the human BRCA2^{MBD} segment containing D2294 residing in the stronger half of the BRCA2 interface with MEILB2$^{83\text{-end}}$ (Fig. 2D and Ext. data fig. 4). As the mutated aspartate residues are expected to bind MEILB2 R204 (the equivalent of human MEILB2 R200) from two different subunits, we asked if simultaneously mutating both aspartates will completely abrogate BRCA2^{MBD} localization at recombination sites. Indeed, the double mutant (D2242R/D2265R) abolished BRCA2^{MBD}'s ability to form punctate foci at recombination nodules, and instead, it showed a diffused distribution within the nucleus (Fig. 4A). The reduced intensities of the BRCA2^{MBD} mutants cannot be attributed to lower protein stability/expression, as the levels of each mutant protein determined via immunoblotting were comparable to that of wild type protein (Ext. data fig. 8A). These data suggest that the salt-bridges between mouse BRCA2^{MBD} D2242R/D2265R and MEILB2 R204 are critical for the accumulation of BRCA2 at meiotic recombination nodules, and disruption of these interactions abrogates proper BRCA2 localization in meiotic cells undergoing HR. Together, our results demonstrate that both halves of the BRCA2^{MBD} peptide need to be disrupted to fully compromise proper MEILB2-BRCA2 localization, consistent with a very robust assembly *in vivo*.

Our structure and biochemical data suggested that BRCA2 binding reinforces MEILB2 quaternary structure, implying that the MEILB2-BRCA2 interaction may also impact MEILB2 function (i.e., localization at recombination nodules). To test this, we introduced GFP fusions of full-length mouse MEILB2 containing W136A, D272R/D330H, and R204D mutations, which correspond to the human MEILB2 W132A, D268R/D326H, and R200D mutations, respectively, at the MEILB2-BRCA2 binding interface. The expression of GFP-MEILB2 proteins demonstrated that the introduction of W136A and D272R/D330H mutations significantly attenuated its recombination nodule localization (71% and 52% reductions, respectively, compared to wild type; Fig. 4B). The R204D mutation, which disrupts two salt-bridges with BRCA2^{MBD}, displayed an even more drastic reduction of signal intensity (95% reduction compared to wild type; Fig. 4B). The residual localization of GFP-MEILB2-R204D in wild type spermatocytes likely results from dimerization with endogenous MEILB2, as this signal was not detected in the *Meilb2*$^{-/-}$ background (Ext. data fig. 8B). These data suggest that electrostatic (mediated by mouse MEILB2 D272, D330, and R204) and stacking (mediated by mouse MEILB2 W136) interactions with BRCA2^{MBD} are also necessary for the localization of MEILB2 to the meiotic recombination sites.

Together, our data suggest that MEILB2 and BRCA2 localize to the meiotic recombination sites in a highly interdependent manner.

We asked if MEILB2 ARM repeat dimerization is necessary for MEILB2 localization *in vivo*. For this, we engineered mouse MEILB2 Δ(87–158), which is equivalent to the human MEILB2 Δ(83–154) truncation mutant that lacks the long N-terminal helix in the MEILB2$^{83\text{-end}}$ homodimerization interface (Fig. 2A). We observed a complete loss of MEILB2 accumulation along the chromosomes in the presence of this mutation, strongly suggesting that MEILB2 ARM dimerization is necessary for proper MEILB2 recruitment to meiotic sites of HR (Ext. data fig. 9A–C). Next, we asked if dimerization afforded by the ARM domain is sufficient to mediate MEILB2 localization. MEILB2 Δ(1–87), which lacks the N-terminal coiled-coil region involved in both dimerization and BRME1 binding, resulted in a dampened MEILB2 signal along the chromosome axes (Ext. data fig. 9D–F). This result is consistent with previous findings[20] and suggests that both the coiled-coil and the ARM domain N-terminus are necessary for proper MEILB2 dimerization and localization to recombination sites. We noted that the mouse MEILB2 C124A, an alanine mutation at the position equivalent to the disulfide-forming C120 residue of human MEILB2 (Fig. 2A,B), did not compromise MEILB2 localization (Ext. data fig. 9A–C). These observations suggest that the MEILB2 coiled-coil and the ARM domain N-terminus together form an extensive dimerization interface *in vivo* that is not weakened by a single (C124A) mutation. Together, our *in vivo* findings highlight the importance of both BRCA2 binding and homodimerization of MEILB2 in ensuring proper MEILB2-BRCA2 recruitment to meiotic sites of recombination.

Discussion

The bridging of two MEILB2 dimers by BRCA2 in a 4:2 stoichiometry is rare among known protein-protein interactions, with the 4:2 coiled-coil interaction between Csm1 and Lrs4 in the yeast monopolin complex involved in sister chromatid co-orientation serving as an example relevant to meiosis[24]. However, within that complex, Lrs4 seems to adopt a tight coiled-coil mediated homodimeric structure, which stands in contrast to the lack of interactions between the two BRCA2^{MBD} subunits in the MEILB2$^{83\text{-end}}$ -BRCA2^{MBD} complex. Receptor tyrosine kinase-ligand interactions represent another well-studied case where binding partners (ligands) either induce homodimerization or bind to pre-formed dimeric receptors[25]. There is an intricate homodimeric interface that either pre-exists or forms in the presence of the ligand for most RTKs. Even in the case of NGFR-NGF, where there is bridging of two (non-dimerized) receptor molecules by the ligand, a homodimeric ligand is employed[26]. In contrast, there is no significant contact between either the two MEILB2$^{83\text{-end}}$ homodimers or the two BRCA2^{MBD} monomers in the 4:2 complex (schematized in Fig. 1E). The complex is formed by the binding of two MEILB2$^{83\text{-end}}$ copies arising from different homodimers to separate segments of a single BRCA2^{MBD} chain (aa 2293–2311 and 2316–2334). Despite sharing no obvious sequence similarity, these two segments of the BRCA2^{MBD} polypeptide adopt near-identical conformations to bind the same groove on two different MEILB2$^{83\text{-end}}$ subunits. This can be inferred from the structural alignment of BRCA2^{MBD}-bound MEILB2$^{83\text{-end}}$ B and A subunits, which not only shows an excellent overlap between the two MEILB2$^{83\text{-end}}$ subunits as expected (Z-score

= 32.3; RMSD = 1.1 Å) but also similar binding modes for both BRCA2^{MBD} segments in the ARM repeat groove of MEILB2$^{83\text{-end}}$ (Fig. 2F,G). The binding of BRCA2^{MBD} in the concave groove of the ARM-repeat domain of MEILB2$^{83\text{-end}}$ is reminiscent of how β-catenin binds its protein partners (Ext. data fig. 3A–C). As the two BRCA2^{MBD} segments lack secondary structural elements when bound to MEILB2$^{83\text{-end}}$, their structural homology is best explained by an induced-fit mechanism of binding to the binding groove in MEILB2$^{83\text{-end}}$.

Our structure demarcates BRCA2^{MBD} sequence into three units with independent structural functions. A short peptide at its very N-terminus (^{2276}PLILVGE^{2282}) is involved in forming lattice contacts (Ext. data fig. 2D,E and Methods). BRCA2^{MBD} aa 2293–2311 uses an extensive surface to bind MEILB2$^{83\text{-end}}$ A/a, and MEILB2$^{83\text{-end}}$ B/b binds to a smaller surface or BRCA2^{MBD} aa 2316–2334 (Fig. 2D–G and Ext. data fig. 4). Remarkably, these three regions are encoded by three separate (and consecutive) exons in the *BRCA2* gene (Fig. 2H). Different domains are often encoded by distinct exons[27], but these BRCA2 regions are neither large nor structured enough to be considered domains. Nevertheless, they represent unique structural motifs that are involved in different aspects of the MEILB2$^{83\text{-end}}$-BRCA2^{MBD} structure.

Strikingly, several identical residues, including R200, D326, and W132, are used by both MEILB2$^{83\text{-end}}$ A and B to bind their respective sites in the BRCA2^{MBD} polypeptide (Fig. 2D). From a functional standpoint, these residues are bifunctional as they have specificity and affinity for two different regions of BRCA2. From an evolutionary perspective, these residues are “doubly” important as their mutation would disrupt interactions with two distinct parts of the binding partner. In other words, covariation in the MEILB2-BRCA2 interface would mandate adaptation at two BRCA2 locations in response to the alteration of one MEILB2 site. These observations are consistent with the strict conservation of these MEILB2 residues and underscore a binding strategy that is unusual among known protein-protein interactions (Ext. data fig. 5I).

Our *in vivo* analysis demonstrates that MEILB2-BRCA2 complex formation is critical for the recruitment of both proteins to meiotic double-stranded breaks. These findings mandate a shift in the paradigm for BRCA2 recruitment to meiotic recombination sites, which previously assumed sequential recruitment of the two proteins based on the loss of proper BRCA2 localization in MEILB2 KO cells[19]. The synergistic recruitment of MEILB2-BRCA2 would allow for the ramping up of BRCA2 recruitment from the basal levels observed in somatic cells to meet the HR demands posed by the plethora of programmed DSBs formed in meiosis (see model below).

Putting our structural findings in the context of what is already known, we propose a model for BRCA2 recruitment to meiotic recombination nodules (Fig. 5). The N-terminal coiled-coil domain of MEILB2 is aggregation-prone, and its binding to BRME1 stabilizes MEILB2 in a homodimeric state[20]. Our structural and functional analyses identify the C-terminal ARM domain of MEILB2 as an additional dimerization module reinforced by binding to BRCA2^{MBD}. The two dimerization modules synergistically ensure MEILB2 dimerization and stabilize the 4:4:2 BRME1-MEILB2-BRCA2 complex at meiotic HR sites. In addition,

the stable association of BRME1-MEILB2-BRCA2 with HR sites will depend on MEIOB-SPATA22, likely through protein-protein interactions[20]. Retention of (a faint) MEILB2-BRME1 localization and appearance of a milder recombinase-recruitment phenotype at recombination sites in *Meiob* KO versus *Meilb2* KO spermatocytes imply the existence of MEIOB-SPATA22-independent pathways to recruit BRME1-MEILB2-BRCA2[20,28]. The ssDNA-binding of the MBD-adjacent OB domains of BRCA2 (Fig. 1A)[29], reinforced by dimerization via binding to BRME1-MEILB2, may provide an additional avenue to recruit BRCA2 to sites of meiotic HR.

Enhanced BRCA2 recruitment facilitated by MEILB2 requires a meiotic context (i.e., presence of meiotic factors like BRME1, MEIOB, and SPATA22)[20,28,30,31] as the exogenous expression of MEILB2 in cultured somatic cells lacking endogenous MEILB2 diminishes HR efficiency[20]. Indeed, inappropriate expression of MEILB2 in somatic cells is a hallmark of several cancers[21]. The robust 4:2 MEILB2-BRCA2 architecture explains how MEILB2 can sequester BRCA2 away from sites of HR in cancer cells in the absence of additional meiotic factors. In conclusion, the MEILB2-BRCA2 complex represents a novel structural scaffold that drives BRCA2 function in meiotic cells, but when hijacked by cancer cells, compromises genome integrity.

Methods

Primers, cDNA, plasmid constructs, site-directed mutagenesis and cloning.

All primers were purchased from IDT. Synthetic cDNA for human MEILB2 and BRCA2^{MBD} were purchased from Genscript. Human MEILB2$^{83\text{-end}}$ and BRCA2^{MBD} (aa 2271–2335) from these cDNA were cloned into the pET Duet vector (Novagen) for co-expression in the *E. coli* BL21 (DE3) strain (Novagen). MEILB2$^{83\text{-end}}$ was cloned downstream of a His-Smt3 tag (that was cloned from the pSmt3 vector obtained upon signing a material transfer agreement with Cornell University;[32]) in the upstream cloning site of the pET Duet vector while tag-free BRCA2^{MBD} was cloned in the downstream cloning site with an in-frame start codon to initiate translation. For expression in HEK 293T cells, MEILB2$^{83\text{-end}}$ was cloned into a pcDNA 3-derived vector with a C-terminal 3X FLAG tag or a 6X myc tag. pcDNA-eGFP-hBRCA2^{MBD}-6xmyc, which encoded an N-terminal dual myc-eGFP tag, was purchased from GenScript. The eGFP was included to increase the molecular weight of the BRCA2 construct to assist membrane transfer and detection by Western blot analysis. Mutations in MEILB2 and BRCA2 were introduced with a QuikChange Site Directed Mutagenesis kit (Agilent) using complementary mutant primers. The presence of the intended mutation was verified by Sanger sequencing. All cloned plasmids were subjected to Sanger sequencing to not only verify the accuracy of the cloned cDNA but to also rule out unintended mutations.

Protein expression and purification

The His-Smt3-hMEILB2$^{83\text{-end}}$ and hBRCA2^{MBD} proteins were co-expressed from the pET-Duet vector (Novagen) in BL21 (DE3) *E.coli* cells after induction with 0.1 mM isopropyl β-D-1-thiogalactopyranoside (IPTG) at 37°C for 3 h. To lyse, cell pellets were resuspended in lysis buffer (25 mM Tris-HCl (pH 7.6), 500 mM NaCl, 10 mM 2-mercaptoethanol,

0.1 mM EDTA, 1 mM PMSF, and 1X protease inhibitor (cOmplete Protease Inhibitor Cocktail, Roche) and sonicated. The lysate was clarified via centrifugation at 30,000 x g for 30 min at 4°C. The clarified supernatant was incubated with nickel-NTA agarose beads (Qiagen) for 2 h at 4°C. Beads were collected by gravity flow and washed twice with wash buffer (25 mM Tri-HCl s (pH 7.6), 150 mM NaCl, 10 mM 2-mercaptoethanol). Beads were then washed with high salt wash buffer (25 mM Tris-HCl (pH 7.6), 300 mM NaCl, 10 mM 2-mercaptoethanol). The proteins co-eluted from nickel-NTA agarose beads (Qiagen) (using buffer containing 25 mM Tris-HCl (pH 7.6), 300 mM NaCl, 10 mM 2-mercaptoethanol supplemented with 500 mM imidazole (pH 8)) consistent with complex formation (as $BRCA2^{MBD}$ was tag-free). The polyHis-Smt3 tag was cleaved by incubating the eluted protein for 15 min at RT with Ulp1 protease (1% of total eluted protein)[32]. For crystallization purposes, the complex was further purified on a cation exchange column (HiTrap SP, GE Healthcare) and finally subjected to size exclusion chromatography (Superdex 200 column, GE Healthcare; buffer containing 25 mM Tris-HCl (pH 7.6), 100 mM NaCl, 2 mM DTT) to obtain an essentially pure complex of the two proteins. For biochemical analysis, the ion exchange step was omitted. Selenomethionine-derivatized complex was co-expressed in the *E.coli* strain B834 (DE3), which is a methionine auxotroph that allows for the incorporation of exogenously supplemented selenomethionine (SeMet) in lieu of methionine in expressed proteins[33]. The cells were grown in SeMet medium base (Molecular Dimensions) supplemented with a SeMet nutrient mix (Molecular Dimensions) following the manufacturer's instructions, and 50 mg l^{-1} SeMet. Cells were induced with IPTG and the protein complex was purified as described above for the native complex.

SEC-MALS

To determine the molar mass of the $MEILB2^{83\text{-}end}$-$BRCA2^{MBD}$ complex, 500–1000 μg of the purified complex was loaded on to a Superdex 200 10/300 size exclusion column (GE Healthcare) that is in line with both a DAWN HELIOS II MALS detector (Wyatt Technology) and an Optilab T-rEX differential refractometer (Wyatt Technology). Differential refractive index and light scattering data were measured, and the data analyzed using the ASTRA 6 software (Wyatt Technology). Extrapolation from Zimm plots was used to calculate molecular weights using a dn/dc value of 0.185 ml g^{-1}.

Structure determination of human $MEILB2^{83\text{-}end}$ bound to human $BRCA2^{MBD}$

Human $MEILB2^{83\text{-}end}$-$hBRCA2^{MBD}$ wild type and Se-Met-containing protein crystals were obtained via vapor diffusion in a hanging drop format using 1 μl protein solution and 1 μl reservoir solution. Crystals obtained in buffer containing 0.1 M sodium acetate (pH 4.6) and 2 M lithium acetate were cryoprotected in buffer containing 0.1 M sodium acetate (pH 4.6) and 2.5 M lithium acetate. While diffraction was obtained with native and Se-Met-containing protein crystals, the highest quality data were obtained with the latter. Therefore, the final structure obtained was that of the Se-Met derivative. Diffraction data were obtained at Argonne National Laboratory on LS-CAT beamline 21 ID-D at a wavelength of 0.97895 Å and a temperature of 100 K. Data were indexed, integrated, and scaled using XDS[34,35]. The phase problem was solved using single-wavelength anomalous diffraction (SAD) with the anomalous signal of selenium atoms. All Se sites in $MEILB2^{83\text{-}end}$ and $BRCA2^{MBD}$ were identified with the exception of the starting selenomethione of $BRCA2^{MBD}$, and

the experimental map was generated using PHENIX Autosol[36]. PHENIX Autobuild[36] was used to build the initial model which was then improved with iterative model building in Coot[37] and model refinement in PHENIX Refine[38]. While non-crystallographic symmetry (NCS) averaging was included during the initial refinement cycles after auto-building, it was removed in subsequent rounds of refinements as the asymmetry of the two MEILB2 subunits in the ASU became clear. The final structure yielded a R/Rfree of 0.2124/0.2310 and good geometry with no amino acids in disallowed regions of the Ramachandran plot. See Table 1 for detailed data statistics. While the ASU consists of two MEILB2$^{83\text{-end}}$ and one BRCA2^{MBD} subunits, PISA analysis of the lattice, SEC-MALS of the complex in solution, and structure validation studies in cultured human cells and mouse spermatocytes, revealed that the biological assembly consists of two ASUs bound to each other related by a crystallographic two-fold symmetry. Contiguous electron density was observed for the BRCA2^{MBD} chain (Ab/aB) for aa 2286–2335 with no obvious density in its vicinity for the region upstream of this residue (aa 2271–2285). However, a short N-terminal peptide of BRCA2^{MBD} (^{2276}PLILVGE^{2282}; annotated as * and shown in black and grey in Fig. 1) was clearly resolved lying antiparallel to the very C-terminus (F2335) of the MEILB2$^{83\text{-end}}$-bound BRCA2^{MBD} chain. The distance between the C-terminus of this short peptide (E2282) and the N-terminus of the BRCA2^{MBD} chain (K2286) is inconsistent with the two polypeptides belonging to the same BRCA2^{MBD} molecule (Ext. data fig. 2D). Inspection of the symmetry mates related by the crystallographic three-fold symmetry (triangular symbol) revealed bridging of three MEILB2$^{83\text{-end}}$ homodimers by three BRCA2^{MBD} chains (composed of aa 2276–2282- - −2286–2335), each of which initiates (aa 2276–2282) adjacent to one MEILB2$^{83\text{-end}}$ homodimer but continues to form the BRCA2^{MBD} chain (aa 2286–2335) of another MEILB2$^{83\text{-end}}$ homodimer (Ext. data fig. 2D). The lattice contacts are mediated by the antiparallel arrangement between the N-terminus (aa 2276–2282) of one BRCA2^{MBD} chain (head) and the C-terminus (aa 2335 and upstream residues) of another BRCA2^{MBD} chain (tail) in the triangular arrangement (Ext. data fig. 2D).

Co-immunoprecipitation

HEK 293T cells were transfected with 1 μg of plasmids containing either wild type or mutant FLAG- MEILB2$^{83\text{-end}}$, myc- MEILB2$^{83\text{-end}}$ or myc-eGFP-BRCA2^{MBD} constructs using Lipofectamine LTX (Invitrogen) transfection reagent using the manufacturer's instructions. 48 h post transfection, the cells were washed with PBS and lysed in lysis buffer (50 mM Tris-HCl (pH 7.4), 20% glycerol, 1 mM ethylenediaminetetraacetic acid (EDTA), 150 mM NaCl, 0.5% Triton X-100, 0.02% sodium dodecyl sulfate (SDS), 1 mM dithiothreitol, 2 mM phenylmethylsulfonyl fluoride (PMSF), and one protease inhibitor cocktail tablet (Roche)) and incubated on ice for 10 min. NaCl concentration was then adjusted to 300 mM and the samples were centrifuged at 16,000 g for 10 min. Input samples were collected and the remaining supernatant was incubated with anti-FLAG M2 affinity gel (Sigma) overnight at 4°C with rocking. Next morning, the FLAG beads were washed three times with lysis buffer and the samples analyzed with SDS-PAGE and immunoblotting. For this, protein samples were separated on SDS-PAGE gels, transferred to a nitrocellulose membrane, and probed with the following antibodies: anti-FLAG M2-HRP conjugate (Sigma, A8592; dilution: 1:10,000) and anti-c-Myc HRP conjugate (Santa Cruz; sc-40 HRP; dilution: 1:5000). Bio-rad Precision Plus Protein Dual Color Standards (in kDa

from top to bottom of gel: 250, 150, 100, 75 (pink), 50, 37, 25 (pink), 20, 15, and 10) were run on all SDS-PAGE gels including those for Western blot analysis and Coomassie-blue staining analysis. FLAG- MEILB2$^{83\text{-end}}$ migrates between the 25 kDa and 37 kDa markers; myc- MEILB2$^{83\text{-end}}$ travels slightly above the 37 kDa marker; and myc-eGFP-BRCA2^{MBD} travels slightly below the 50 kDa marker (see uncropped and unprocessed images in Source Data files).

Mice

Knockout mice for *Meilb2* were reported previously[19]. Wild type and knockout mice were congenic with the *Mus musculus* C57BL/6J background. Only male mice were used as studies were done in spermatocytes. All animal experiments were approved by and done in compliance with the regulations at the University of Gothenburg Institutional Animal Care and Use Committee (#1316/18).

Antibodies

The following antibodies were used: rabbit antibodies against GFP (Invitrogen; A11122); mouse antibodies against β-Actin (Sigma; A2228–100UL); and chicken antibody against SYCP3[19].

Exogenous protein expression in the testis

Plasmid DNA was electroporated into live mouse testes as previously described[39]. Briefly, male mice at PD16–30 were anesthetized with pentobarbital, and the testes were pulled from the abdominal cavity. Plasmid DNA (10 μl of 5 μg/μl solution) was injected into each testis using glass capillaries under a stereomicroscope (M165C; Leica). Testes were held between a pair of tweezers-type electrodes (CUY21; BEX), and electric pulses were applied four times and again four times in the reverse direction at 35 V for 50 ms for each pulse. The testes were then returned to the abdominal cavity, and the abdominal wall and skin were closed with sutures. The testes were removed 24 h after the electroporation, and immunostaining was performed.

Immunostaining of spermatocytes

Testis cell suspensions were prepared by mincing the tissue with flathead forceps in PBS, washing several times in PBS, and resuspending in a 1:1 mixture of PBS and hypotonic buffer (30 mM Tris-HCl (pH 7.5), 17 mM trisodium citrate, 5 mM EDTA, 2.5 mM DTT, 0.5 mM PMSF, and 50 mM sucrose). After 10 min, the sample was centrifuged and the supernatant was aspirated. The pellet was resuspended in a 1:2 mixture of PBS and 100 mM sucrose. A total of 20 μl of fixation buffer (1% paraformaldehyde, 0.15% Triton X-100, and 1 mM sodium borate (pH 9.2 adjusted by NaOH)) was applied to a glass slide, and 3 μl of the cell suspension was added to the drop, allowed to fix for 1 h at room temperature, and air-dried. For immunostaining, the slides were incubated with primary antibodies in PBS containing 5% BSA for 2 h and then with Alexa Fluor 488- or 594- conjugated secondary antibodies (1:1,000 dilution, Invitrogen) for 1 h at room temperature. The slides were washed with PBS and mounted with VECTASHIELD medium with DAPI (Vector Laboratories). All antibodies used in in vivo studies were used in 1:1000 dilution.

Microscopy

Images were obtained on a microscope (Olympus IL-X71 Delta Vision; Applied Precision) equipped with 100× NA 1.40 objective, a camera (CoolSNAP HQ; Photometrics), and softWoRx 5.5.5 acquisition software (Delta Vision). Images were processed with Photoshop (Adobe).

Extended Data

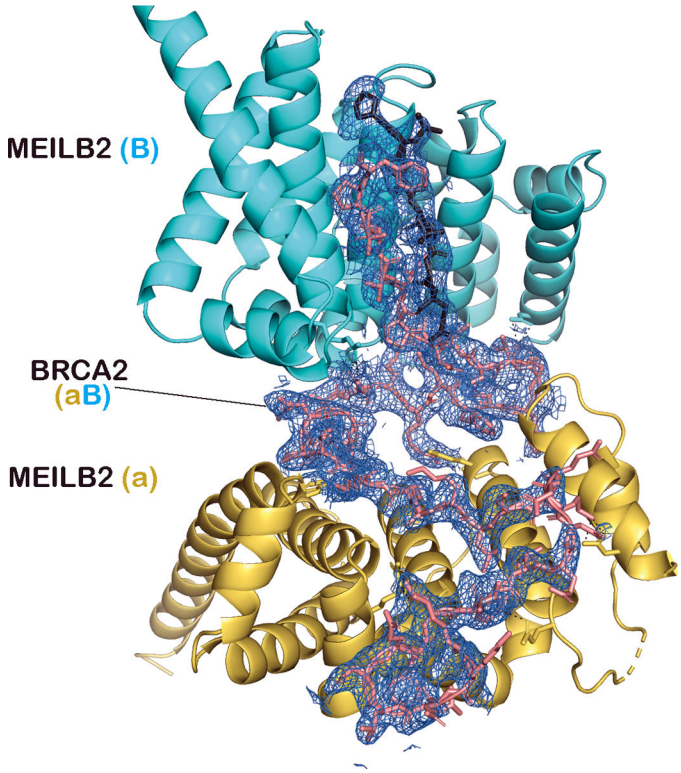

Extended Data Fig. 1. Electron density for BRCA2^{MBD}

The sandwich between MEILB2$^{83\text{-end}}$ a and B subunits, and BRCA2^{MBD} is shown in cartoon representation along with $2F_o$-F_c electron density map encompassing BRCA2^{MBD} contoured at 1.0 σ.

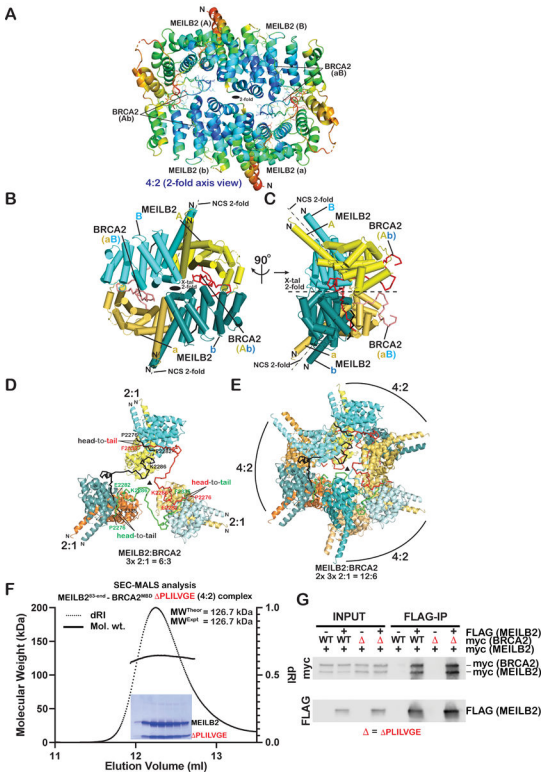

Extended Data Fig. 2. MEILB2-BRCA2 quaternary structure

(A) B-factor heat map (blue→red indicates low→high B-factors) for the MEILB2$^{83\text{-end}}$-BRCA2^{MBD} complex highlighting the ordered nature of the MEILB2-MEILB2 and MEILB2-BRCA2 interfaces. (B) Back view and (C) side view (right) of the human MEILB2$^{83\text{-end}}$-BRCA2^{MBD} complex (relative to depictions in Figure 1) shown in cartoon representation. Note in panel C how the NCS two-fold axis of MEILB2$^{83\text{-end}}$ homodimerization is oblique (i.e., neither parallel nor perpendicular) with respect to the crystallographic two-fold axis of 4:2 complex formation. (D) Head-to-tail anti-parallel alignments of the N-terminus of one BRCA2^{MBD} chain (aa 2276–2282; head) and the C-terminus of another BRCA2^{MBD} chain (aa 2335 and upstream residues; tail) in the crystal lattice results in the formation of a triangular 6:3 MEILB2$^{83\text{-end}}$-BRCA2^{MBD} assembly from three 2:1 complexes around the three-fold crystallographic axis. (E) Further inclusion of the symmetry mates related by the two-fold crystallographic axis results in a 12:6 assembly in the crystal lattice. (F) SEC-MALS analysis of MEILB2$^{83\text{-end}}$ - BRCA2^{MBD} ΔPLILVGE strongly suggests formation of a 4:2 complex. (G) Anti-FLAG co-immunoprecipitation (co-IP) analysis of HEK 293T cell lysates containing transiently transfected FLAG-tagged MEILB2$^{83\text{-end}}$, myc-tagged MEILB2$^{83\text{-end}}$ and either eGFP-myc-vector control, eGFP-myc-tagged BRCA2^{MBD} wild type, or eGFP-myc-tagged BRCA2^{MBD} ΔPLILVGE constructs. Data are representative of three replicates.

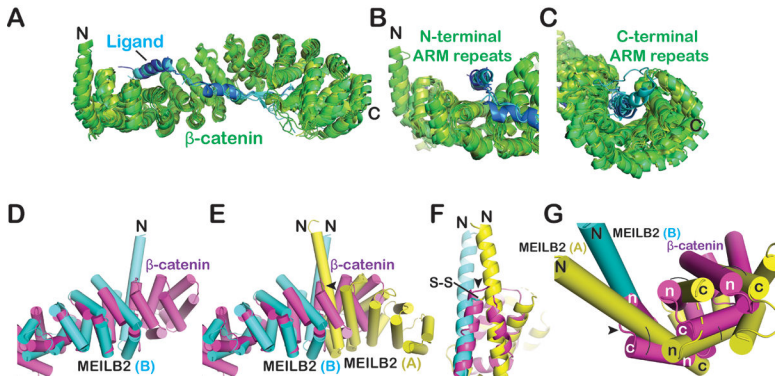

Extended Data Fig. 3. MEILB2 ARM repeat domain structure and homodimerization is an adaptation of the extensive ARM repeat structure of β-catenin

(A) Overlay of 9 different ligand-bound β-catenin structures in the PDB showing the ligands tracing the concave track formed by tandem ARM repeats. β-catenin and its binding partners from the various structures are shown in different shades of green and blue, respectively. (B-C) Closeup of the partner-bound concave surfaces at the N-terminal (B) and C-terminal (C) ARM repeats of β-catenin. PDB IDs: 1qz7, 1jdh, 3ouw, 1jpp, 1g3j, 2g17, 1i7x, 1i7w, and 1jpw. (D) Alignment of the MEILB2$^{83\text{-end}}$ B subunit with its top DALI server alignment hit, β-catenin (PDB ID: 1i7w). (E) Alignment of MEILB2$^{83\text{-end}}$ B with β-catenin as in panel D but also showing the homodimeric partner MEILB2$^{83\text{-end}}$ A subunit that was not used in the alignment. (F) The hairpin connecting two helices of β-catenin that align with the N-terminal helices of MEILB2$^{83\text{-end}}$ A and B is structurally replaced by the disulfide linkage between the MEILB2$^{83\text{-end}}$ subunits. (G) The helices of the N-terminal ARM repeat of MEILB2$^{83\text{-end}}$ A superimpose with β-catenin regions but the polarity of the helices (n→c) is reversed. Curved lines indicate the superimposed helices of β-catenin and MEILB2$^{83\text{-end}}$ A. Arrowhead indicates disulfide linkage.

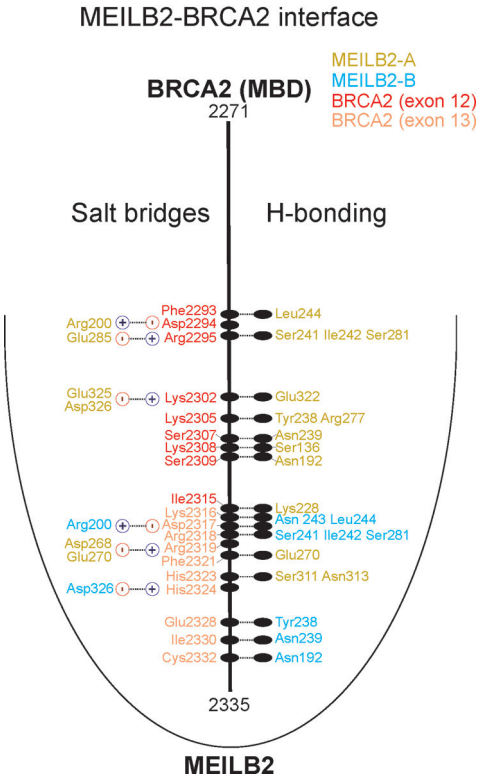

Extended Data Fig. 4. Schematic showing the polar interactions between the BRCA2^{MBD} and its two MEILB2 binding partners

Ionic (salt-bridge; *left*) and H-bonding (*right*) interactions along the entire BRCA2^{MBD} chain is shown schematically. MEILB2 and BRCA2 color-coding is retained from structural depictions in main and other supplementary figures.

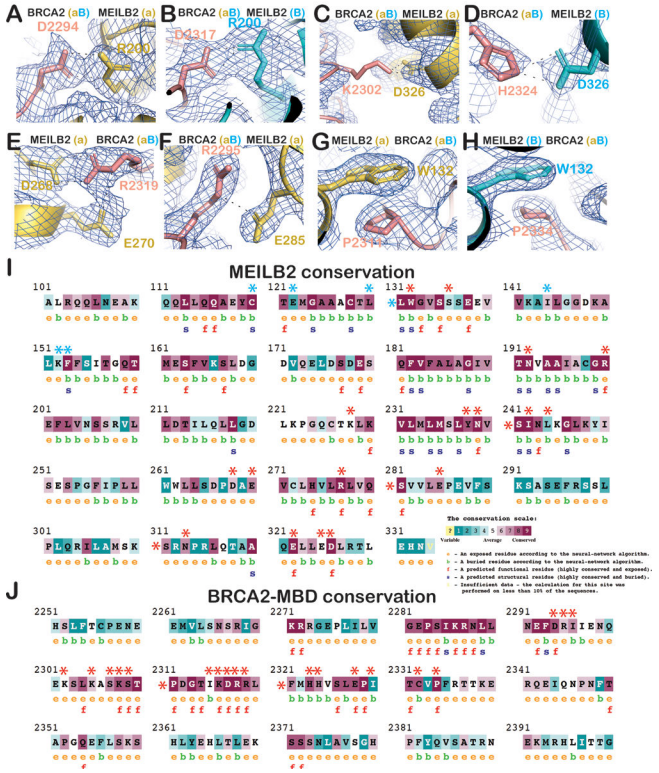

Extended Data Fig. 5. Salt-bridges dominate the MEILB2-BRCA2 interface

(A-H) $2F_O$-F_C electron density map contoured at 1.0 σ and stick representations for the indicated interactions at the MEILB2-BRCA2 interface. (I-J) Consurf analysis of MEILB2$^{83\text{-end}}$ (I) and BRCA2^{MBD} (J) showing the high level of conservation of the MEILB2-MEILB2 (blue asterisks) and MEILB2-BRCA2 (red asterisks) interface residues.

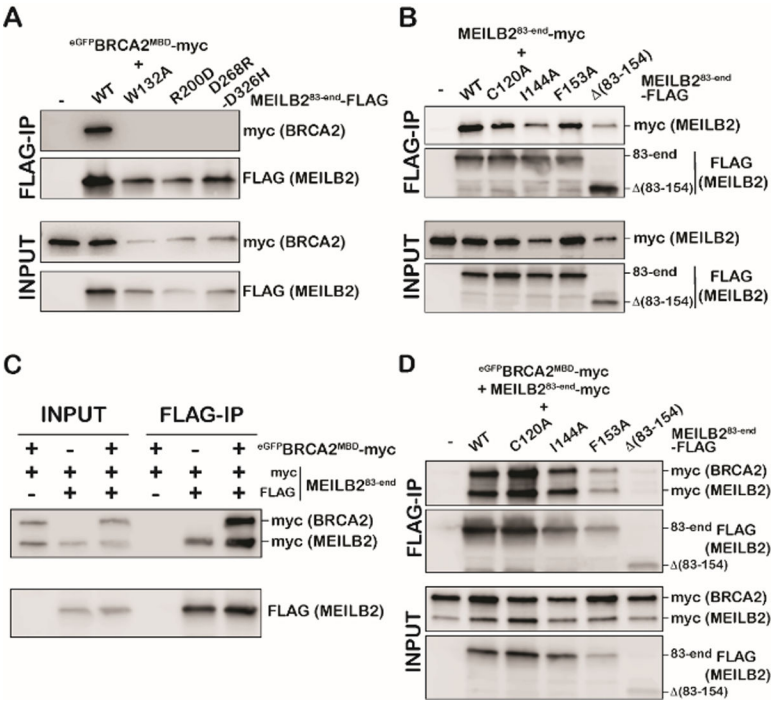

Extended Data Fig. 6. The MEILB2-MEILB2 interface is bolstered by BRCA2

(A) Co-IP analysis of MEILB2$^{83\text{-end}}$ – BRCA2^{MBD} in the presence of MEILB2 mutations including the D268R/D326R double mutant. (B) Anti-FLAG co-immunoprecipitation (co-IP) analysis of HEK 293T cell lysates containing the indicated transiently transfected with wild type myc-tagged MEILB2$^{83\text{-end}}$ and indicated FLAG-tagged MEILB2$^{83\text{-end}}$ constructs harboring mutations in the MEILB2$^{83\text{-end}}$ homodimerization interface. (C) Co-IP analysis of MEILB2-MEILB2 association in the absence and presence of BRCA2^{MBD}. (D) Co-IP of MEILB2$^{83\text{-end}}$ homodimerization mutants in the presence of wild type myc-tagged MEILB2$^{83\text{-end}}$. WT: wild type. Data are representative of at least three replicates.

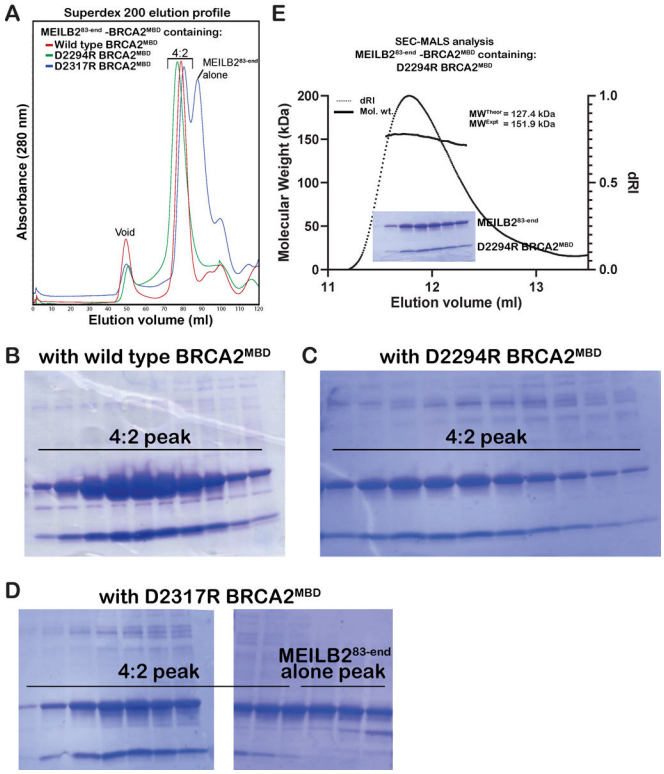

Extended Data Fig. 7. Biochemical analysis of single-mutations in each half of the MEILB2-binding segments of BRCA2^{MBD}

(A) Size-exclusion profiles of purified human MEILB2$^{83\text{-end}}$ -BRCA2^{MBD} complexes containing either wild type, D2294R or D2317R BRCA2^{MBD} subunits. (B-D) Coomassie-stained SDS-PAGE analysis of fractions for the size-exclusion analysis shown in panel A. (E) SEC-MALS of purified human MEILB2$^{83\text{-end}}$-BRCA2^{MBD} D2294R rules out complete dissociation of MEILB2$^{83\text{-end}}$ -BRCA2^{MBD} or dissociation into smaller (i.e., 2:1) complexes; dRI: differential Refractive Index. MEILB2$^{83\text{-end}}$-BRCA2^{MBD} D2317R could not be analyzed by SEC-MALS because of closely eluting BRCA2^{MBD}-complexed and free MEILB2 peaks (seen in panel A). WT and mutant complexes were expressed and purified in the same experiment. WT complex has been purified for more than three times while the two mutant complexes were purified once.

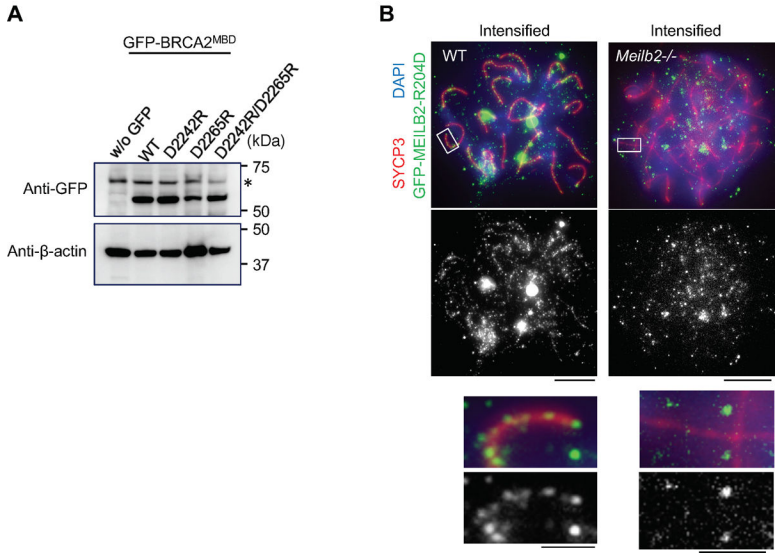

Extended Data Fig. 8. BRCA2^{MBD} and MEILB2 interaction is indispensable for their recombination nodule localization

(A) Immunoblot of testis extracts after electroporating GFP-BRCA2^{MBD} wild type (WT) or indicated mutants, probed with the indicated antibodies. Asterisks indicate non-specific bands. GFP and actin blots in each lane correspond to the same processed sample run on the same gel but blotted sequentially after stripping. (B) Immunostaining of WT and *Meilb2*$^{-/-}$ mouse spermatocytes expressing GFP-MEILB2 WT and R204D mutant protein. Note that axis-associated foci seen in WT were not detectable in *Meilb2*$^{-/-}$ spermatocytes even after the intensification of the signals. Scale bars: 5 μm in the main panel and 1 μm in the magnified panel. Data are representative of two repeats.

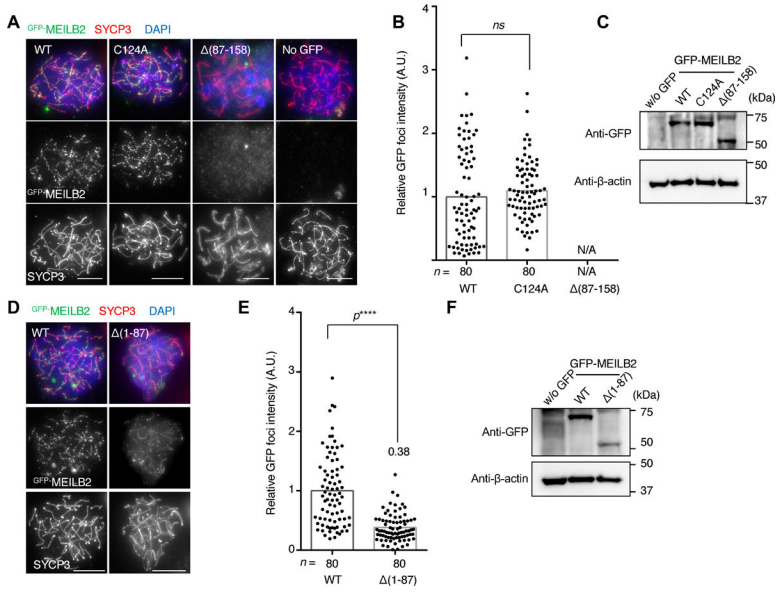

Extended Data Fig. 9. Protein expression and localization of the MEILB2 dimerization mutants

(A) and (D) Immunostaining of WT spermatocytes expressing indicated GFP-MEILB2 WT and mutant proteins. (B) and (E) Quantification of GFP foci intensities represented in panel

A and panel D, respectively, normalized with the average value of WT. n shows the analyzed foci number pooled from four cells from one electroporated mouse. All analyses used two-tailed t-tests. ****$p < 0.0001$ (WT vs. Δ1–87: 1.81285×10^{-14}). Scale bars: 5 μm. (C) and (F) Immunoblots of testis extracts after electroporating indicated GFP-MEILB2 WT and mutant proteins, blotted with the indicated antibodies (repeated two times). GFP and actin blots in each lane correspond to the same processed sample run on the same gel but blotted sequentially after stripping.

Supplementary Material

Refer to Web version on PubMed Central for supplementary material.

Acknowledgements.

We thank Dr. Joseph S. Brunzelle at the Life Sciences Collaborative Access Team (LS-CAT) beam line of the Argonne National Laboratory for help with X-ray diffraction data collection and initial processing; the University of Michigan Structural Biology Supergroup for helpful suggestions; Valerie M. Tesmer of the Nandakumar lab for help with harvesting of crystals and input on figures; and the members of the Nandakumar laboratory for critical feedback on the manuscript. This work was supported by NIH Grants R01-AG050509 (J.N.), R01-GM120094 (J.N.), an American Cancer Society Research Scholar grant RSG-17-037-01-DMC (J.N.), American Heart Association predoctoral fellowship (R.A.), Assar Gabrielsson's Foundation FB-20–57 (J.Z.), the European Research Council StG-801659 (H.S.), the Swedish Research Council 2018–03426 (H.S.), and Cancerfonden 2018/326 (H.S.), and the Knut och Alice Wallensbergs Stiftelse KAW2019.0180 (H.S.).

Data availability:

Coordinates and structure factors of the $MEILB2^{83\text{-end}}$-$BRCA2^{MBD}$ crystal structure are deposited in the protein data bank (PDB) under the accession code 7LDG.

References

1. Kowalczykowski SC & Eggleston AK Homologous pairing and DNA strand-exchange proteins. Annu Rev Biochem 63, 991–1043, doi:10.1146/annurev.bi.63.070194.005015 (1994). [PubMed: 7979259]
2. West SCMolecular views of recombination proteins and their control. Nat Rev Mol Cell Biol4, 435–445, doi:10.1038/nrm1127 (2003). [PubMed: 12778123]
3. San Filippo J, Sung P & Klein H Mechanism of eukaryotic homologous recombination. Annu Rev Biochem 77, 229–257, doi:10.1146/annurev.biochem.77.061306.125255 (2008). [PubMed: 18275380]
4. Pellegrini L & Venkitaraman A Emerging functions of BRCA2 in DNA recombination. Trends in biochemical sciences 29, 310–316, doi:10.1016/j.tibs.2004.04.009 (2004). [PubMed: 15276185]
5. Moynahan ME & Jasin M Mitotic homologous recombination maintains genomic stability and suppresses tumorigenesis. Nat Rev Mol Cell Biol 11, 196–207, doi:10.1038/nrm2851 (2010). [PubMed: 20177395]
6. Zhao W, Wiese C, Kwon Y, Hromas R & Sung P The BRCA Tumor Suppressor Network in Chromosome Damage Repair by Homologous Recombination. Annu Rev Biochem 88, 221–245, doi:10.1146/annurev-biochem-013118-111058 (2019). [PubMed: 30917004]
7. Li ML & Greenberg RA Links between genome integrity and BRCA1 tumor suppression. Trends in biochemical sciences 37, 418–424, doi:10.1016/j.tibs.2012.06.007 (2012). [PubMed: 22836122]
8. Wooster R & Weber BL Breast and ovarian cancer. N Engl J Med 348, 2339–2347, doi:10.1056/NEJMra012284 (2003). [PubMed: 12788999]
9. Stracker TH & Petrini JH The MRE11 complex: starting from the ends. Nat Rev Mol Cell Biol 12, 90–103, doi:10.1038/nrm3047 (2011). [PubMed: 21252998]

10. Syed A & Tainer JA The MRE11-RAD50-NBS1 Complex Conducts the Orchestration of Damage Signaling and Outcomes to Stress in DNA Replication and Repair. Annu Rev Biochem 87, 263–294, doi:10.1146/annurev-biochem-062917-012415 (2018). [PubMed: 29709199]
11. Wold MSReplication protein A: a heterotrimeric, single-stranded DNA-binding protein required for eukaryotic DNA metabolism. Annu Rev Biochem66, 61–92, doi:10.1146/annurev.biochem.66.1.61 (1997). [PubMed: 9242902]
12. Neale MJ & Keeney S Clarifying the mechanics of DNA strand exchange in meiotic recombination. Nature 442, 153–158, doi:10.1038/nature04885 (2006). [PubMed: 16838012]
13. Scully R, Panday A, Elango R & Willis NA DNA double-strand break repair-pathway choice in somatic mammalian cells. Nat Rev Mol Cell Biol 20, 698–714, doi:10.1038/s41580-019-0152-0 (2019). [PubMed: 31263220]
14. Zickler D & Kleckner N Recombination, Pairing, and Synapsis of Homologs during Meiosis. Cold Spring Harb Perspect Biol 7, doi:10.1101/cshperspect.a016626 (2015).
15. Hassold T & Hunt P To err (meiotically) is human: the genesis of human aneuploidy. Nat Rev Genet 2, 280–291, doi:10.1038/35066065 (2001). [PubMed: 11283700]
16. Keeney S, Giroux CN & Kleckner N Meiosis-specific DNA double-strand breaks are catalyzed by Spo11, a member of a widely conserved protein family. Cell 88, 375–384, doi:10.1016/s0092-8674(00)81876-0 (1997). [PubMed: 9039264]
17. Lange Jet al.The Landscape of Mouse Meiotic Double-Strand Break Formation, Processing, and Repair. Cell167, 695–708 e616, doi:10.1016/j.cell.2016.09.035 (2016). [PubMed: 27745971]
18. Robert Tet al.The TopoVIB-Like protein family is required for meiotic DNA double-strand break formation. Science351, 943–949, doi:10.1126/science.aad5309 (2016). [PubMed: 26917764]
19. Zhang J, Fujiwara Y, Yamamoto S & Shibuya H A meiosis-specific BRCA2 binding protein recruits recombinases to DNA double-strand breaks to ensure homologous recombination. Nature communications 10, 722, doi:10.1038/s41467-019-08676-2 (2019).
20. Zhang Jet al.The BRCA2-MEILB2-BRME1 complex governs meiotic recombination and impairs the mitotic BRCA2-RAD51 function in cancer cells. Nature communications11, 2055, doi:10.1038/s41467-020-15954-x (2020).
21. Brandsma Iet al.HSF2BP Interacts with a Conserved Domain of BRCA2 and Is Required for Mouse Spermatogenesis. Cell reports27, 3790–3798 e3797, doi:10.1016/j.celrep.2019.05.096 (2019). [PubMed: 31242413]
22. Krissinel E & Henrick K Inference of macromolecular assemblies from crystalline state. J Mol Biol 372, 774–797, doi:10.1016/j.jmb.2007.05.022 (2007). [PubMed: 17681537]
23. Shahid Tet al.Structure and mechanism of action of the BRCA2 breast cancer tumor suppressor. Nat Struct Mol Biol21, 962–968, doi:10.1038/nsmb.2899 (2014). [PubMed: 25282148]
24. Corbett KDet al.The monopolin complex crosslinks kinetochore components to regulate chromosome-microtubule attachments. Cell142, 556–567, doi:10.1016/j.cell.2010.07.017 (2010). [PubMed: 20723757]
25. Endres NF, Barros T, Cantor AJ & Kuriyan J Emerging concepts in the regulation of the EGF receptor and other receptor tyrosine kinases. Trends in biochemical sciences 39, 437–446, doi:10.1016/j.tibs.2014.08.001 (2014). [PubMed: 25242369]
26. Wiesmann C, Ultsch MH, Bass SH & de Vos AM Crystal structure of nerve growth factor in complex with the ligand-binding domain of the TrkA receptor. Nature 401, 184–188, doi:10.1038/43705 (1999). [PubMed: 10490030]
27. Liu M & Grigoriev A Protein domains correlate strongly with exons in multiple eukaryotic genomes--evidence of exon shuffling? Trends in genetics : TIG 20, 399–403, doi:10.1016/j.tig.2004.06.013 (2004). [PubMed: 15313546]
28. Souquet Bet al.MEIOB targets single-strand DNA and is necessary for meiotic recombination. PLoS Genet9, e1003784, doi:10.1371/journal.pgen.1003784 (2013). [PubMed: 24068956]
29. Thorslund Tet al.The breast cancer tumor suppressor BRCA2 promotes the specific targeting of RAD51 to single-stranded DNA. Nat Struct Mol Biol17, 1263–1265, doi:10.1038/nsmb.1905 (2010). [PubMed: 20729858]

30. Luo Met al.MEIOB exhibits single-stranded DNA-binding and exonuclease activities and is essential for meiotic recombination. Nature communications4, 2788, doi:10.1038/ncomms3788 (2013).

31. Ishishita S, Matsuda Y & Kitada K Genetic evidence suggests that Spata22 is required for the maintenance of Rad51 foci in mammalian meiosis. Scientific reports 4, 6148, doi:10.1038/srep06148 (2014). [PubMed: 25142975]

32. Mossessova E & Lima CD Ulp1-SUMO crystal structure and genetic analysis reveal conserved interactions and a regulatory element essential for cell growth in yeast. Mol Cell 5, 865–876, doi:S1097–2765(00)80326–3 [pii] (2000). [PubMed: 10882122]

33. Leahy DJ, Hendrickson WA, Aukhil I & Erickson HP Structure of a fibronectin type III domain from tenascin phased by MAD analysis of the selenomethionyl protein. Science 258, 987–991, doi:10.1126/science.1279805 (1992). [PubMed: 1279805]

34. Kabsch W Xds. Acta Crystallogr D Biol Crystallogr 66, 125–132, doi:10.1107/S0907444909047337 (2010). [PubMed: 20124692]

35. Kabsch WIntegration, scaling, space-group assignment and post-refinement. Acta Crystallogr D Biol Crystallogr66, 133–144, doi:10.1107/S0907444909047374 (2010). [PubMed: 20124693]

36. Adams PDet al.PHENIX: a comprehensive Python-based system for macromolecular structure solution. Acta Crystallogr D Biol Crystallogr66, 213–221, doi:10.1107/S0907444909052925 (2010). [PubMed: 20124702]

37. Emsley P & Cowtan K Coot: model-building tools for molecular graphics. Acta Crystallogr D Biol Crystallogr 60, 2126–2132, doi:10.1107/S0907444904019158 (2004). [PubMed: 15572765]

38. Afonine PVet al.Towards automated crystallographic structure refinement with phenix.refine. Acta Crystallogr D Biol Crystallogr68, 352–367, doi:10.1107/S0907444912001308 (2012). [PubMed: 22505256]

39. Shibuya H, Morimoto A & Watanabe Y The dissection of meiotic chromosome movement in mice using an in vivo electroporation technique. PLoS Genet 10, e1004821, doi:10.1371/journal.pgen.1004821 (2014). [PubMed: 25502938]

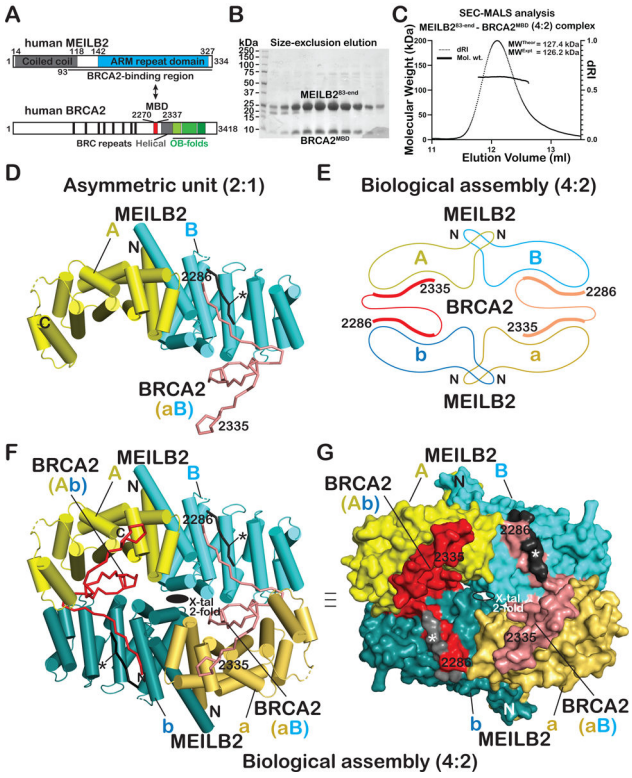

Figure 1. BRCA2 is sandwiched between two MEILB2 homodimers.

(A) Domain diagrams of human MEILB2 and BRCA2. Double-arrow: MEILB2- and BRCA2-interacting regions; MBD: MEILB2-binding domain. The N-terminal coiled coil domain of MEILB2 facilitates homodimerization and BRME1 binding. (B) Coomassie-blue stained SDS-PAGE showing co-elution of human MEILB2$^{83\text{-end}}$ and BRCA2^{MBD} during size exclusion chromatography (SEC). The purification of this complex was performed successfully for greater than three times. (C) SEC-MALS of purified human MEILB2$^{83\text{-end}}$-BRCA2^{MBD} reveals a molar mass consistent with a 4:2 stoichiometry; dRI: differential Refractive Index. (D) Cartoon representation of the asymmetric unit (ASU) of the human MEILB2$^{83\text{-end}}$-BRCA2^{MBD} complex. The ASU contains a homodimer of MEILB2$^{83\text{-end}}$ (between subunits “A” and “B”) and one copy of BRCA2^{MBD} bound to MEILB2$^{83\text{-end}}$ B. (E) Schematic, (F) cartoon representation, and (G) surface representation of the biological assembly formed by two ASUs related by a crystallographic two-fold axis of symmetry (“X-tal 2-fold”; oval). In the 4:2 complex, The “AB” and “ab” homodimers of MEILB2$^{83\text{-end}}$ are bridged by two BRCA2^{MBD} chains. BRCA2^{MBD} (aB) bridges MEILB2$^{83\text{-end}}$ a and B, while BRCA2^{MBD} (Ab) bridges MEILB2$^{83\text{-end}}$ A and b. A short peptide (^{2276}PLILVGE^{2282}; *; black and grey) derived from the N-terminus of another BRCA2^{MBD} chain in the lattice forms lattice contacts (see Ext. data fig. 1E,F and Methods) and it is omitted in the schematic for clarity. “N” indicates MEILB2$^{83\text{-end}}$ N-terminus.

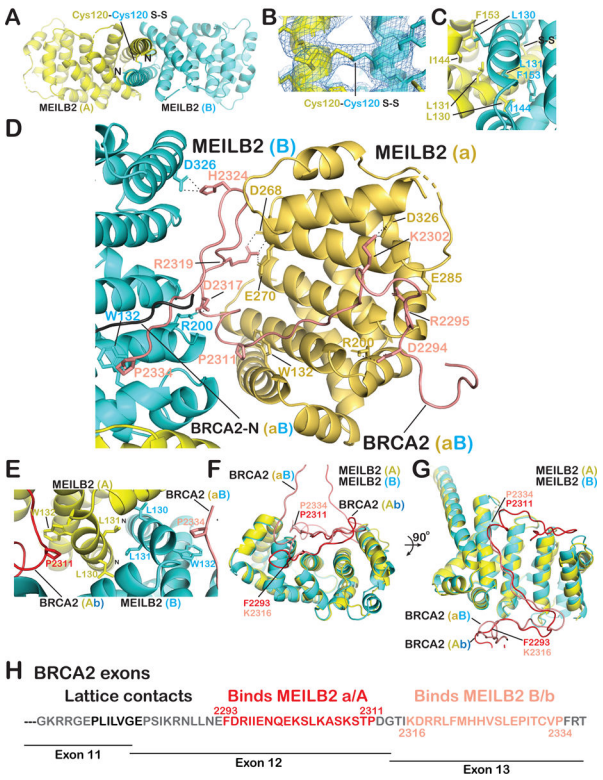

Figure 2. Hydrophobic MEILB2-MEILB2 and an ionic MEILB2-BRCA2 interfaces drive formation of the 4:2 complex.

(A) Cartoon depiction of the ASU viewed through the two-fold non-crystallographic symmetry axis (NCS) showing the N-terminally mediated dimeric interface and presence of a cys-cys disulfide linkage. "N" indicates MEILB2$^{83\text{-end}}$ N-terminus. (B) $2F_o$-F_c electron density map contoured at 1.0 σ across the Cys120-Cys120 disulfide linkage. (C) Strictly hydrophobic homodimerization interface between the N-terminal helix of each subunit and the first ARM repeat of the other subunit. (D) The interactions between BRCA2^{MBD} and the MEILB2$^{83\text{-end}}$ a and B subunits are dominated by the salt-bridges mediated through charged residues shown in the stick representation. MEILB2$^{83\text{-end}}$ W132 mediates stacking interactions with proline residues in BRCA2^{MBD}. MEILB2$^{83\text{-end}}$ R200, D326, and W132 are bifunctional as their counterparts in MEILB2$^{83\text{-end}}$ a and B subunits bind distinct residues of the same BRCA2^{MBD} chain. (E) The W132-P2311 and W132-P2334 MEILB2-BRCA2 interactions mediated by the two BRCA2^{MBD} chains bracket the hydrophobic core of the MEILB2$^{83\text{-end}}$ homodimeric interface. (F-G) Superposition of the A and B monomers of the MEILB2$^{83\text{-end}}$ homodimer, each bound to its BRCA2^{MBD} chain (aB and Ab). Only the MEILB2$^{83\text{-end}}$ chains were used to align the two MEILB2-BRCA2 complexes. Regions K2316-P2334 of BRCA2^{MBD} chain aB and F2293-P2311 of BRCA2^{MBD} chain Ab superimpose well on each other and bind the same groove on their respective MEILB2$^{83\text{-end}}$ partners. F and G represent orthogonal views. (H) The BRCA2^{MBD} structure can be divided into distinct segments that are encoded by separate exons.

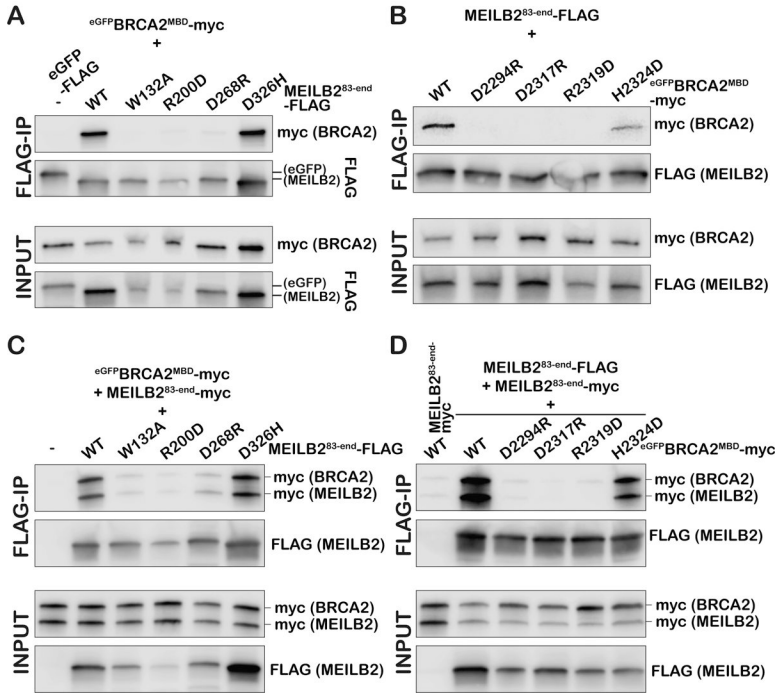

Figure 3. The MEILB2-BRCA2 assembly falls apart in the presence of mutations at the MEILB2-BRCA2 interface.

(A-B) Anti-FLAG co-immunoprecipitation (co-IP) analysis of HEK 293T cell lysates containing the indicated transiently transfected eGFP-myc-tagged BRCA2^{MBD} and FLAG-tagged MEILB2$^{83\text{-}end}$ constructs harboring mutations in the MEILB2-BRCA2 interface. (C-D) Co-IP analysis of MEILB2-BRCA2 interface mutants as in panels A-B but also including myc-tagged MEILB2$^{83\text{-}end}$. WT: wild type. Data are representative of at least three replicates.

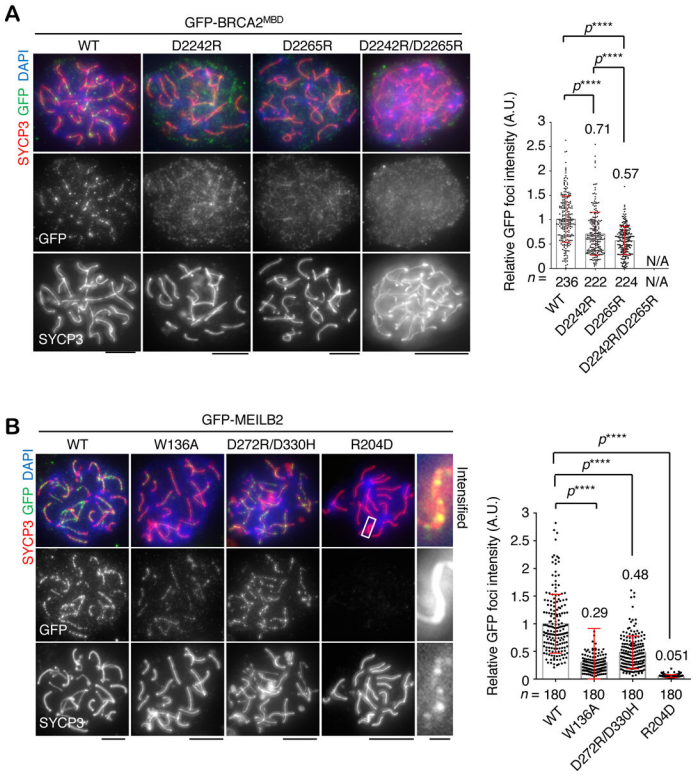

Figure 4. Mutations at the MEILB2-BRCA2 interface compromise recruitment of both proteins to recombination nodules in mouse spermatocytes.

(A) Immunostaining of wild type spermatocytes expressing GFP-tagged BRCA2^{MBD} wild type (WT) and indicated mutant proteins. Graph: the quantification of GFP foci intensities normalized with the average value of WT. Red bars: mean value with SD. *n* shows the analyzed foci number pooled from ten cells from three electroporated mice. Note that D2242R/D2265R did not form discernable foci. (B) Immunostaining of WT spermatocytes expressing GFP-tagged MEILB2 WT and indicated mutant proteins. Graph: the quantification of GFP foci intensities normalized with the average value of WT. Red bars: mean value with SD. *n* shows the analyzed foci number pooled from twelve cells (panel A) or nine cells (panel B) from three electroporated mice. All analyses used two-tailed *t*-tests. ****$p < 0.0001$ (Panel A: WT vs. D2242R: 1.09376×10^{-11}; WT vs D2265R: 1.39094×10^{-28}; D2242R vs. D2265R: 8.89428×10^{-5}. Panel B: WT vs. W136A: 1.52767×10^{-26}; WT vs. D272R/D330H: 6.30641×10^{-26}; WT vs. R204D: 5.83804×10^{-76}). Scale bars: 5 μm in the main panels and 0.5 μm in the magnified panels.

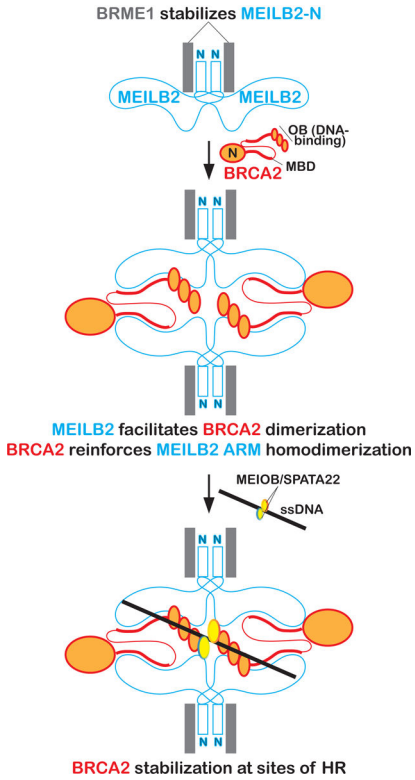

Figure 5. Model for BRCA2 recruitment to sites of meiotic HR.

BRME1 binding binds the N-terminus of MEILB2 to stabilize it and facilitate dimerization using coiled-coil interactions. Binding of BRCA2^{MBD} to MEILB2 helps form a BRME1:MEILB2:BRCA2 4:4:2 complex that reinforces MEILB2 ARM domain dimerization and facilitates BRCA2 dimerization. Dimeric BRCA2 bound to MEILB2 and BRME1 is stably recruited to sites of meiotic HR in the presence of the ssDNA-binding MEIOB-SPATA22 complex using protein-protein interactions as well as BRCA2-OB-mediated protein-DNA interactions.

Table 1:

Data collection and refinement statistics for SeMet-derivatized MEILB2$^{83\text{-end}}$-BRCA2^{MBD} crystals.

	MEILB2$^{83\text{-end}}$-BRCA2^{MBD} selenomethionine derivative (PDB accession code: 7LDG)
Data collection	
Space group	R 3 2 :H
Cell dimensions	
a, *b*, *c* (Å)	179.889 179.889 179.186
α, β, γ (°)	90 90 120
Wavelength (Å)	0.97895
Resolution (Å)	89.94 – 2.56 (2.7 – 2.56)
R_{merge}	0.088 (1.467)
$CC_{1/2}$	0.999 (0.833)
$I / \sigma I$	18.9 (2)
Overall Completeness (%)	100 (100.00)
Anomalous Completeness (%)	100 (100.00)
Redundancy	21 (21.7)
Refinement	
Resolution (Å)	31.1 – 2.56 (2.651 – 2.56)
No. reflections	35987 (3546)
R_{work} / R_{free}	0.2106 (0.3027) / 0.2307 (0.3496)
No. atoms	3812
Protein	3806
Ligand/ion	0
Water	6
B-factors	96.72
Protein	96.72
Water	91.77
R.m.s deviations	
Bond lengths (Å)	0.004
Bond angles (°)	0.611
Ramachandran favored (%)	97.48
Ramachandran allowed (%)	2.52
Ramachandran outliers (%)	0.00

Structure was solved with data from a single SeMet derivative. Values in parentheses are for highest-resolution shell.